

Electronic Supplementary Information (ESI) for Chemical Communications

Crystal Facet Modulation of Bi₂WO₆ Microplates for Spatial Charge Separation

Abraham Adenle,^{ab} Hongpeng Zhou,^a Xiaoping Tao,^a Yue Zhao,^a Ming Shi,^{ab} Bin Zeng,^{ab} Jiangshan Qu,^{ab} Rengui Li,^{*a} and Can Li^{*a}

Experimental Section

Sample Preparation

All starting chemicals used in this work are of analytical grade and utilized without further treatments. Bi₂WO₆ microplate sample was prepared using flux treatment method. In a typical synthetic procedure, stoichiometric ratios of Bi₂O₃ (99.0 %, Beijing Shiji) and WO₃ (99.0 %, Beijing Shiji) with single flux or eutectic mixture of NaCl (99.5 %, Sinopharm Chemical) and KCl (99.5 %, Sinopharm Chemical) as flux were mixed using mortar and pestle in the presence of absolute ethanol as solvent. After thorough mixing and solvent evaporation, the mixture was transfer into alumina crucible and heat in air at 923 K for 3 h in a temperature-programmed oven. The obtained cool product was washed several times with deionize warm water and dried in the oven at 80 °C overnight. For the thickness modulation, different Bi₂WO₆ samples namely, S1, S2, S3, S4, S5 and S6 were prepared under the same reaction conditions with single flux or eutectic mixture of flux ratio. Specifically, 5.0 mmol Bi₂O₃ and 5.0 mmol WO₃ with different flux ratio were use as the starting precursor; S1 (25.0 mmol NaCl); S2 (25.0 mmol KCl); S3 (50.0 mmol NaCl); S4 (50.0 mmol KCl); S5 (50.0 mmol NaCl:50.0 mmol KCl) and S6 (100.0 mmol NaCl:100.0 mmol KCl) were thoroughly mixed in the presence of ethanol and heat at 923 K for 3 h in the air.

Characterization

The as-prepared Bi₂WO₆ crystal structure was characterized using X-ray diffraction (XRD) on a Rigaku D/Max-2500/PCXRD (Bruker D8) and the UV-visible (UV-vis) diffuse reflectance spectra were recorded on a UV-vis spectrophotometer (JASCO V-550). The microstructure and morphology of the samples are examined on (SEM, Quanta 200 FEG, FEI) coupled with energy-dispersive X-ray spectroscopy (EDX) and high-resolution transmission electron microscopy (HRTEM, TECNAI G2 F30). The photoelectron spectroscopy (XPS) was carried out on an ESCALAB 250Xi instrument (Thermo Fisher, UK). Raman spectra analysis was measure on the Renishaw company spectrograph with a spectral resolution of 2 cm⁻¹. The laser line at 532 nm was use as the exciting source. The power of the laser line, measured at the samples was about 0.3 mW and the spectra of all samples were record at room temperature. Nitrogen adsorption-desorption measurement was conducted at 77 K on a Quantachrome Novawin analyzer version 11.02 after samples were degassed at 363 K for 2 h. Transient photocurrent response and electrochemical impedance spectroscopy are measured using an electrochemical workstation and Versa-studio- C-V (CHI-760D, Chenhua Instruments Co., Ltd.) with 0.10 M Kpi, phosphate buffer as the electrolyte at 0.6V vs RHE. A saturated calomel electrode and platinum (Pt) wire were use as the reference electrode and counter electrode respectively, the fabricated Bi₂WO₆ electrode was use as working electrodes. Photoelectrochemical measurements are carry out under simulated solar-light irradiation (300 W xenon lamp).

Evaluation of photocatalytic performances

The photocatalytic O₂ evolution performance of the as-prepared Bi₂WO₆ samples were carried out in a vacuum, in a closed gas circulation and evacuation system under visible light, using a 300 W Xe lamp (Ushio-CERMAX LX300) and an optical cutoff filter (kenko, L42, λ ≥ 420 nm). Specifically, 100 mg of the as-prepared photocatalyst was dispersed in 100 mL H₂O containing 1.0 mM Fe(NO₃)₃ in a Pyrex reaction cell. The air in the reaction system was absolutely removed to make sure that the system is well vacuum, and the amount of O₂ produced was determine by an on-line gas chromatograph (Agilent, GC-7890, TCD, Ar carrier). The rate of O₂ evolution in the initial 1 h was use for evaluating the photocatalytic activity of the Bi₂WO₆ samples. In the same manner, photocatalytic water oxidation was carried out on S5 microplate to study the effect of facet-selective deposition of reduction and oxidation co-catalyst. The contents of the cocatalysts are 0.2 wt. % RuO₂ and 0.5 wt. % Ag regardless of the deposition method.

Photocatalytic Fe³⁺ ion conversion

Photocatalytic Fe³⁺ ion conversion efficiency of the as-prepared Bi₂WO₆ samples in methanol and water were determined using an open system under visible light, with a 300 W Xe lamp (Ushio-CERMAX LX300) and an optical cutoff filter (kenko, L42, λ ≥ 420 nm). Specifically, for Fe³⁺ ion conversion efficiency in methanol, 100 mg of the photocatalyst was dispersed in 20% methanol solution in a 250 mL conical flask, follow by the addition of 5.0 mM Fe(NO₃)₃ and the prepared solution was placed in a cooling water bath and irradiated from the top under magnetic stirring. 1.0 mL of the irradiated solution was collected at 30 minutes interval and the Fe²⁺ ions in solution were quantitatively determined using phenanthroline method. The same procedure was adopted for Fe³⁺ ion conversion efficiency during water oxidation. The quantitative amount of Fe²⁺ ion in solution was determined

using phenanthroline method. Precisely, the solution after reaction was dilute such that the concentration of Fe^{2+} is less than 1.0 mM. Then 1.0 mL diluted solution was mixed with 4.0 mL 0.2 M NaAc-HAc buffer solution (pH=4.0) and 3.0 mL 0.1 wt % 1, 10-phenanthroline solution (50 vol % ethanol solution). The UV-Vis absorption spectrum was measured and the concentration of Fe^{2+} was calculated according to the absorbance at 510 nm using a calibration curve.

Apparent quantum efficiency measurement

The apparent quantum efficiency (AQE) measurement was carried out in pyrex-5 top-irradiation-type reaction vessel and evacuation system, using 300 W Xe lamp as light source (Ushio-CERMAX LX300). Band-pass filters (Asahi Spectra Co., FWHM: 10 nm) with λ at 420 was used. The number of photons reaching the reaction solution was measured using a calibrated Si photodiode (LS-100, EKO Instruments Co., LTD.) and the AQE (%) was calculated according to the following equation:

$$AQE(\%) = (AR/I) \times 100$$

where A, R, and I represent coefficient for O_2 evolution, oxygen evolution rate in the initial one hour of irradiation, and the absorption rate of incident photons, respectively. The total number of incident photons at the wavelength of 420 nm and 380 nm was measure to be 8.69×10^{20} photons h^{-1} and 5.11×10^{20} photons h^{-1} .

Photo-deposition of metals and metal oxides

Facet selective photo-deposition of metal and or metal oxide were carried out as reported.¹ In a typical preparation method, reduction and oxidation cocatalyst were singly and simultaneously deposited on the different facets of the prepared Bi_2WO_6 photocatalyst in a vacuum at room temperature without change in pH value. Specifically, 0.50 g Bi_2WO_6 photocatalysts powder and calculated amount of metal precursor are mix in 100 mL deionized water, and the suspensions are illuminated continuous stirring for 4 h under visible light. Metal oxides particles are deposited from MnCl_2 and $\text{Pb}(\text{NO}_3)_2$ under the same condition as above with NaIO_3 as electron capture, likewise metallic reduction cocatalyst was deposited from using HAuCl_4 , H_2PtCl_6 or AgNO_3 . After photo-deposition, the obtained products were filter and wash several times with deionize water and dried at 80 °C overnight.

Fabrication of Bi_2WO_6 electrode

FTO substrates were wash three times under ultra-sonication with deionized water and absolute ethanol before drop coating of the prepared mixture on the conductive glass. In a typical fabrication procedure, a thin film of photocatalyst (Bi_2WO_6) on the substrate was achieved by mixing (20 mg) of photocatalyst and 10 mg PVP (MW: 10000) in 1.0 mL ethyl alcohol as solvent (99.7%, Sinopharm Chemical). The obtained mixture was drop coated on FTO substrate with pipette and spread using a glass-rod. The obtained thin-film electrode was dry at room temperature and calcined in air at 623 K for 2 h.

DFT calculations

The DFT method was employed to investigate surface electronic properties and surface energy using Vienna Ab Initio Simulation Package (VASP)² with the projector-augmented wave (PAW) method.³ For all the calculations, we used generalized gradient approximation of Perdew-Burke-Ernzerh of (GGA-PBE) as the exchange-correlation potential.⁴ The slabs with 72 atoms (3 conventional cell) and 15 Å of vacuum layer were fully relaxed until the force on each ion were converted to less 0.05 eV Å⁻¹, and the cutoff energy for plane wave basis set was 520 eV. The Hubbard Correction U was applied on the W d states (U = 6.2 eV) to obtain more accurate electronic properties and energy of ground state.

The surface energy (γ) was determined using the following equation.⁵

$$\gamma = \frac{\left(E_{slab} - \frac{N}{n} E_{bulk} \right)}{2A}$$

where E slab is the DFT energy of given facet, E bulk is for the total DFT energy of bulk structure (n = 24 atoms), N is the number of atoms in a surface slab (n = 72 atoms), n is the number of atoms in the bulk unit cell (n = 24 atoms), and A is the area of the given surface slab. The schematic illustrations of the perfect unit cell of the bulk and two surface slabs ({010} and {001}) have are shown in Fig. S18.

To elucidate the facet-dependent charge separation, the surface work function was calculated according to electrostatic potential method using VASP code.¹⁰ The electrostatic potential is defined as the sum of the ionic and Hartree potentials. The fluctuations of electrostatic potential correspond to the charge variation of lattice atoms. Firstly, we can create a slab structure contain a vacuum layer and calculate the planar ($\bar{V}(z)$) or macroscopic ($\tilde{V}(z)$) average electrostatic potential along vacuum direction.¹¹

$$\bar{V}(z) = \frac{1}{S} \iint_S V(r) dx dy \quad (1)$$

$$\tilde{V}(z) = \frac{1}{L} \int_{-L/2}^{L/2} V(z) dz \quad (2)$$

Where $V(r)$ is electrostatic at position $r(x,y,z)$ in slab structure. x, y, z represents coordination along the a, b, c lattice axis of slab structure, respectively. As shown in Fig. S16, the fluctuations and flat region of electrostatic potential curves represent slab structure and vacuum layer (Fig. S18), respectively. Then, the fermi level value reference electrostatic can be extracted (Fig. S16, dash line).¹⁰

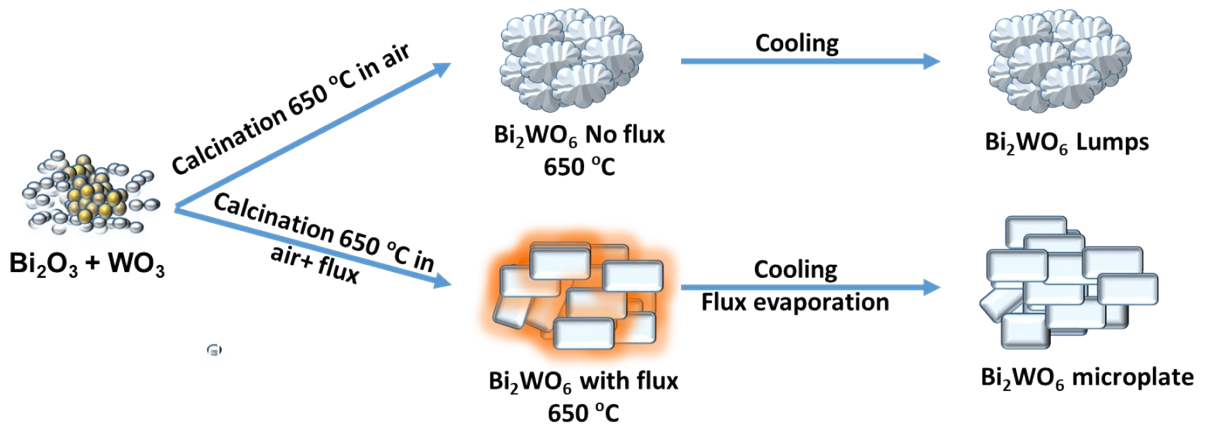


Fig.S1 Schematic illustration of Bi_2WO_6 formation mechanism

Fig.S1 shows Bi_2WO_6 crystal growth mechanism using flux method. According to the scheme above, well-define Bi_2WO_6 crystal are grow by the dissolution of flux precursor at high temperature followed by cooling and flux evaporation process. Typically, at the initial stage, accurately measured precursor and flux are place in high temperature stable refractory container. At elevated temperature, flux solution dissolves the charge forming homogeneous precursor before nucleation and growth of crystals take place under appropriate saturated. During the cooling process, the flux evaporate and the different morphology are form. Significantly, type of flux and the flux concentration determined the morphology formation process.

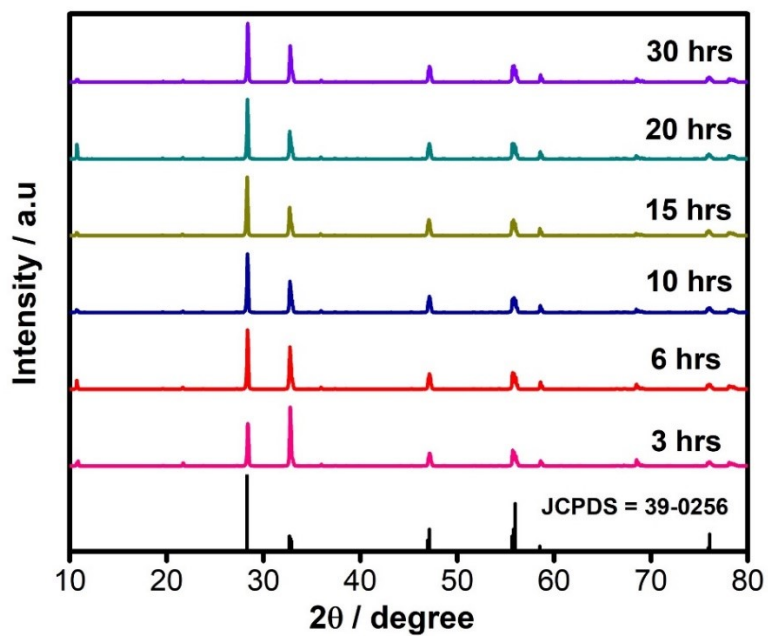


Fig. S2 XRD pattern of Bi₂WO₆ samples obtained for optimizing reaction time for the preparation of well-defined Bi₂WO₆ photocatalyst.

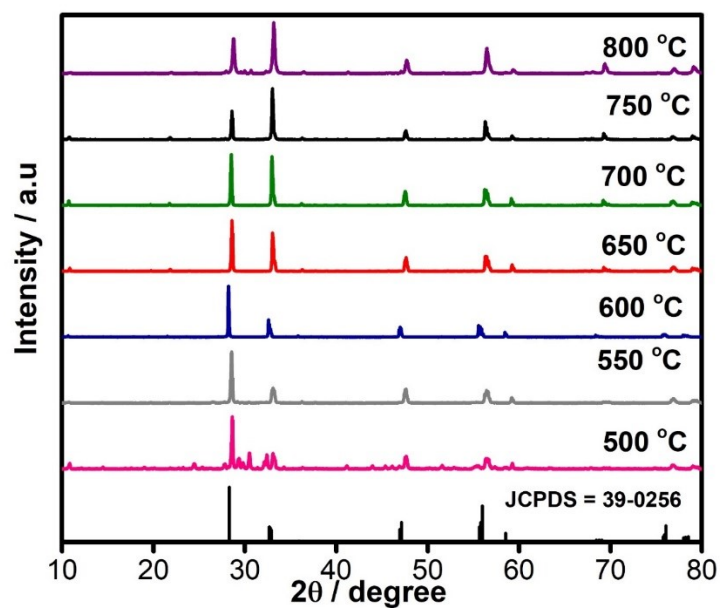


Fig. S3 XRD patterns of Bi₂WO₆ samples obtained for optimized reaction temperature for the preparation of well-defined Bi₂WO₆ photocatalyst.

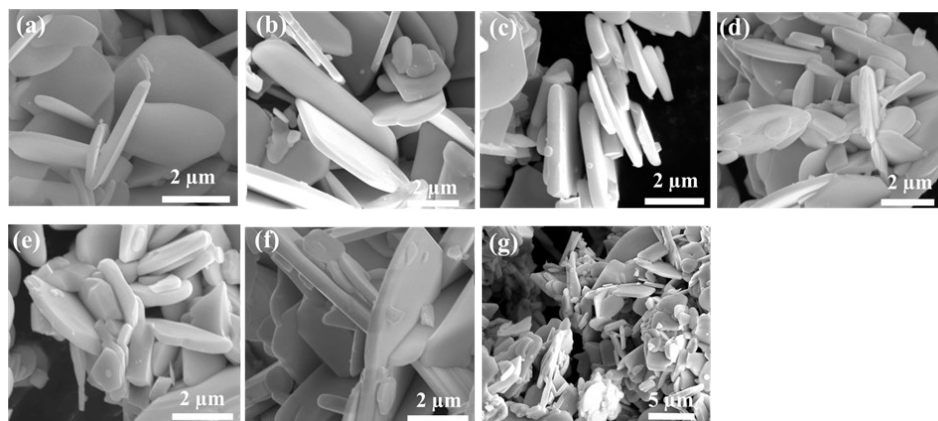


Fig. S4 SEM images of Bi₂WO₆ samples obtained for optimizing reaction time at a fixed temperature of 650 °C over different time. (a) 3 h; (b) 6 h; (c) 10 h; (d) 15 h; (e) 20 h; (f) 30 h and (g) 40 h.

In order to optimize the reaction time for the preparation of a well-define Bi₂WO₆ microplate crystal, time dependent reactions were carried out. No significant change can be observed in the XRD pattern as shown in Fig.S2 above, all samples matched perfectly with the standard Card. However, a gradual significant change in particles shapes with non-uniform microplate and increase in particle size along the reaction time range can be observed in the SEM images. This observation justifies the importance of carrying out the time dependent preparation of Bi₂WO₆ to obtain the best reaction time.

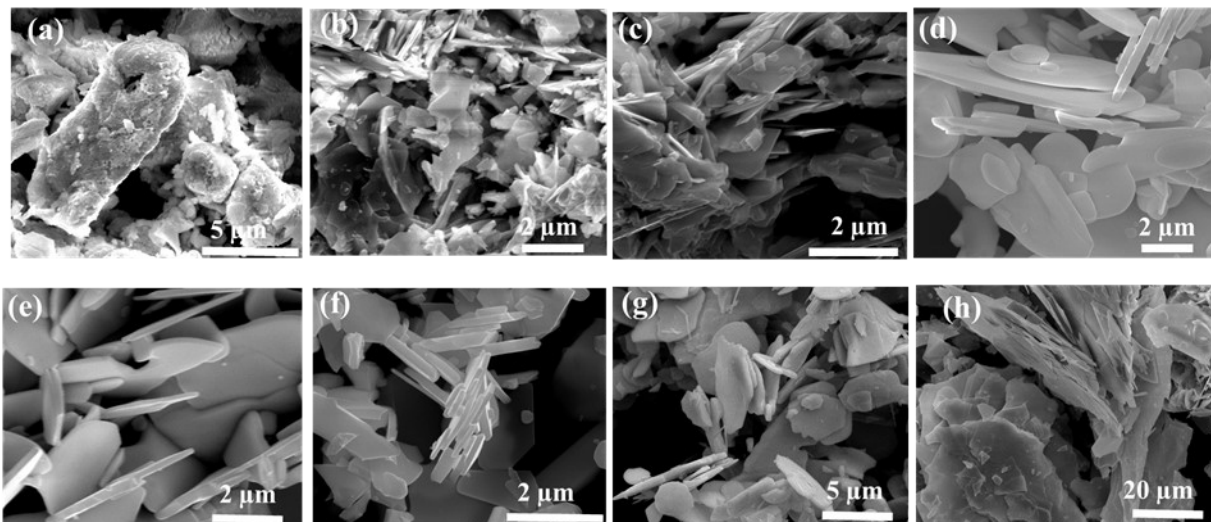


Fig. S5 SEM images of Bi₂WO₆ samples prepared at different temperatures. (a) 500 °C; (b) 550 °C; (c) 600 °C; (d) 650 °C; (e) 700 °C; (f) 750 °C and (g) 800 °C.

Furthermore, the reaction temperature for the preparation of well-define Bi₂WO₆ using flux method was carry out. Fig. S5 shows SEM images of temperature dependent reaction carried to obtain a suitable reaction temperature. As revealed above, an obvious significant change can be observed over the different reaction temperature for the preparation of well-define Bi₂WO₆. It is revealed that, at 500 °C coagulated large crystal of Bi₂WO₆ with impurity phase can be obtain as revealed by the XRD pattern in Fig.S3 above. Nevertheless, further preparation at more elevated temperature shows that an irregular microplate crystal with several nanoparticles can be obtain. An increase in the temperature between 600 °C to 700 °C leads to the formation a regular microplate crystal. It is therefore revealing that consideration should be given to optimizing the reaction conditions for the preparation of regular well-define Bi₂WO₆ facets.

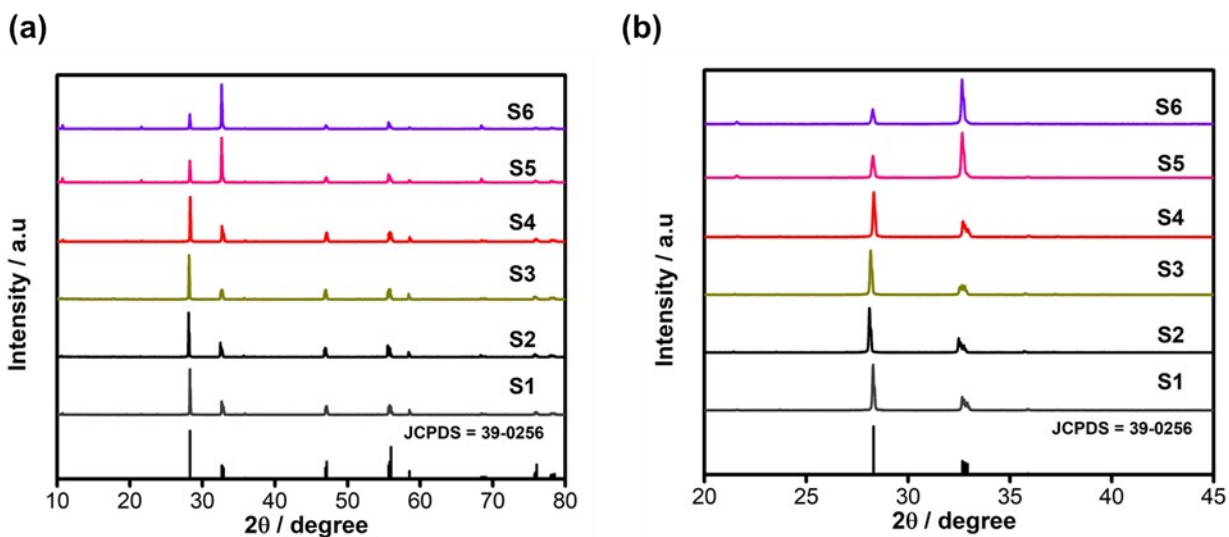


Fig. S6 (a, b) XRD and expanded XRD patterns of Bi₂WO₆ samples S1-S6 and inset standard card.

Well-defined Bi₂WO₆ microplates named samples S1-S6 were prepared using flux method (Fig.S1) based on the reaction temperature and time optimization (Fig. S2-S5). A typical synthesis process includes that stoichiometric ratio of Bi₂O₃ and WO₃ (1:1) with single flux or eutectic mixture of flux (NaCl and KCl) was mixed with ethanol as solvent. After thorough mixing and subsequent solvent evaporation, the mixture was transferred into alumina crucible and heated at 923K in air for 3 h. Thereafter, the obtained cool product was washed several times with deionized warm water and dried at 80 °C in oven overnight. XRD characterization of the as-prepared samples (S1-S6) were conducted as shown in Fig. S6, all of the characteristic peaks are assigned to orthorhombic russellite Bi₂WO₆ (JCPDS card No.39-0256) without any impurities. It is noteworthy that relative peak intensity apparently varies with the changes in flux ratios, with the ratio of (200) plane gradually increasing from sample S1 to S6, indicating an obvious change in the morphology and the corresponding exposed crystal facets. Scanning electron microscopy (SEM) characterization shows that all of Bi₂WO₆ samples comprised of uniform microplate (Fig. 1d-1i) with the thickness orderly decreasing from more than 500 nm for S1 to 160 nm for S6, which agrees with the decrease of particle size (Table S1). These results show the adjustability of crystal facets of Bi₂WO₆ microplate through flux treatment. However, to further justify the importance of flux in the preparation of well-defined Bi₂WO₆ microplate, sample without flux was also prepared for comparison (Fig. S7), which comprise of irregular particles.

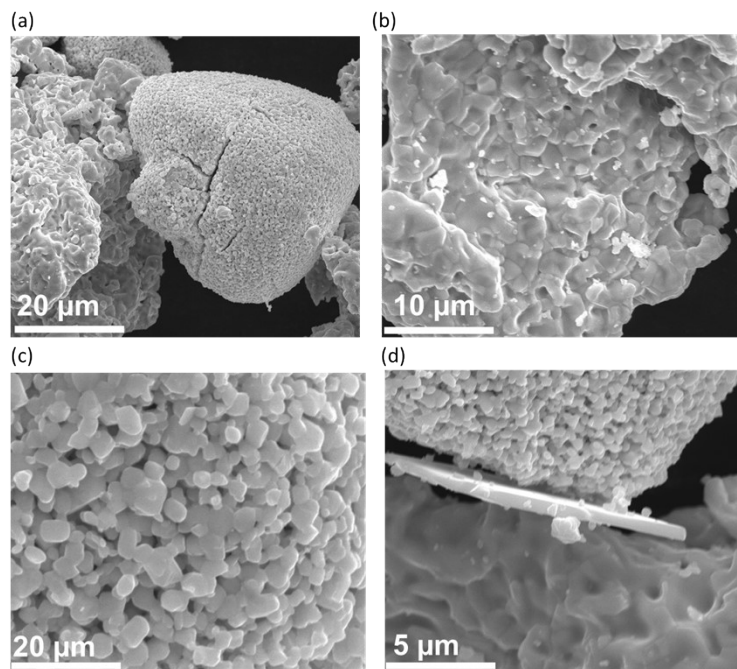


Fig. S7 SEM image of Bi_2WO_6 prepared without flux under the same condition as S1-S6.

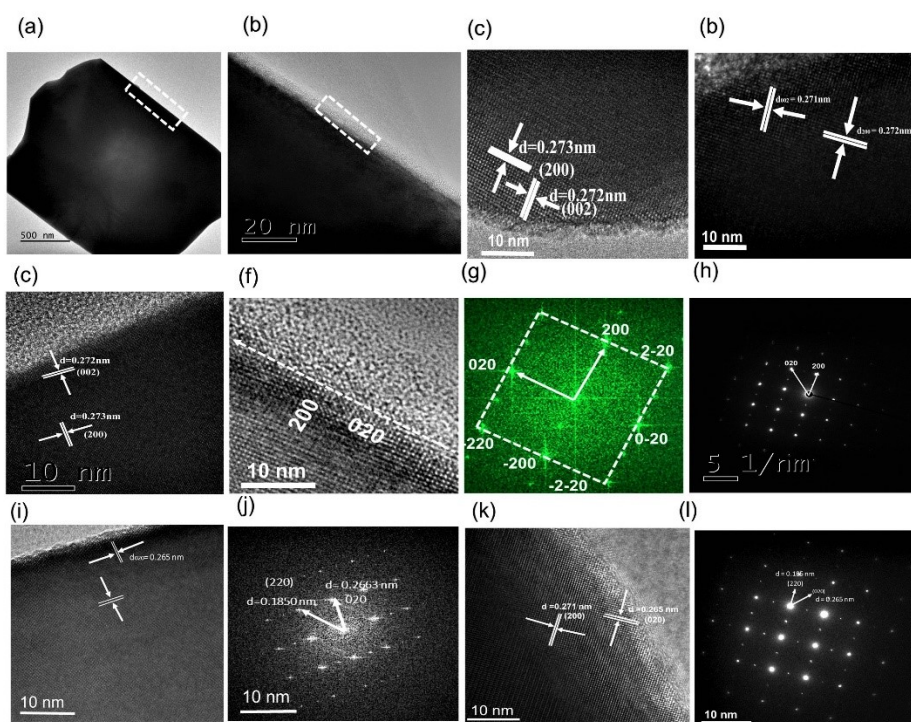


Fig. S8 (a, b) TEM images of Bi_2WO_6 microplate, (c-i) HRTEM and FFT images of Bi_2WO_6 S5 microplate with $\{100\}$, $\{100\}$ exposed edge facet and $\{100\}$ exposed top facet (zone axis 001).

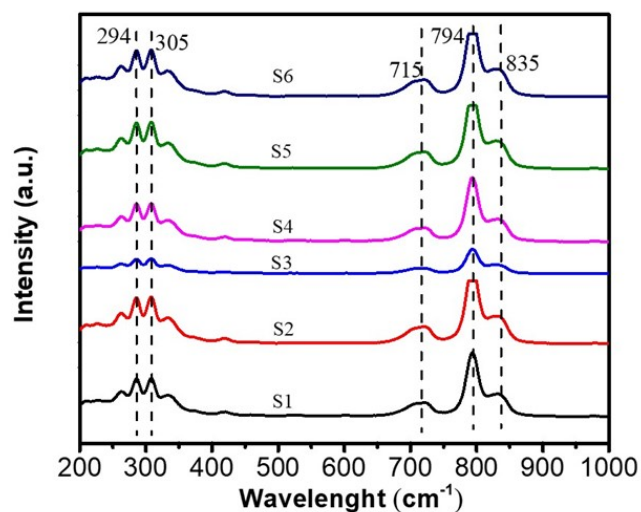


Fig. S9 Raman spectral of Bi_2WO_6 (S1-S6) samples prepared under the same reaction condition. It shows major band at 835 cm^{-1} , 794 cm^{-1} and 714 cm^{-1} attributed to antisymmetric and symmetric modes of terminal O-W-O modes. The peaks at about 305 cm^{-1} and 294 cm^{-1} are assign to translation modes involving simultaneous motion of Bi^{3+} and W-O.

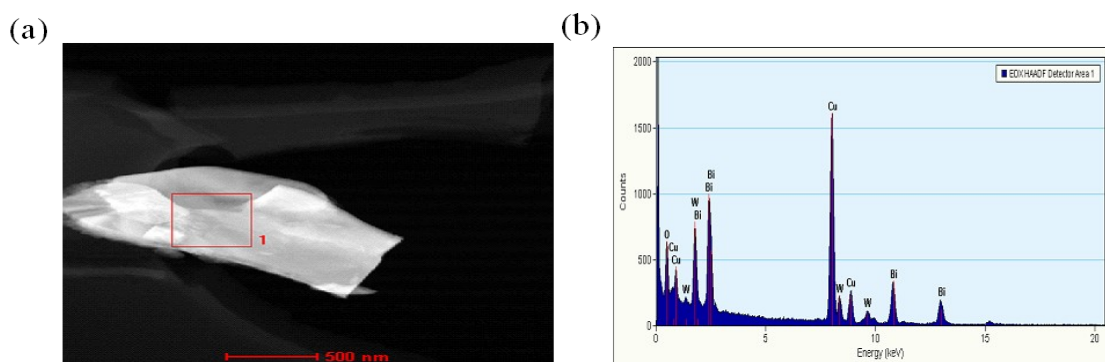


Fig. S10 Elemental analysis by energy dispersive spectroscopy (EDX) of Bi_2WO_6 . (a) Selected area of Bi_2WO_6 and (b) elemental analysis spectrum.

As demonstrated in Fig.S10, the EDX analysis further confirm the preparation of Bi_2WO_6 photocatalyst. However, a strong peak of Cu can be observed from Fig. S10b, originating from the sample grid used for sample TEM analysis.

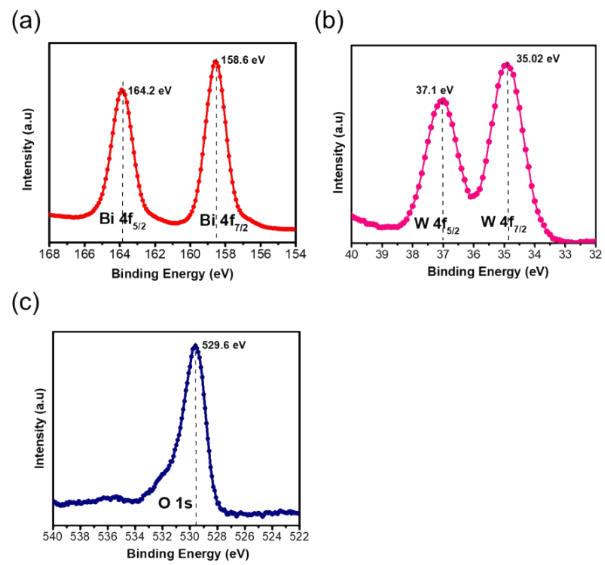


Fig. S11 High-resolution XPS spectra of (a) Bi 4f, (b) W 4f and (c) O 1s of the flux prepared Bi_2WO_6 photocatalyst.

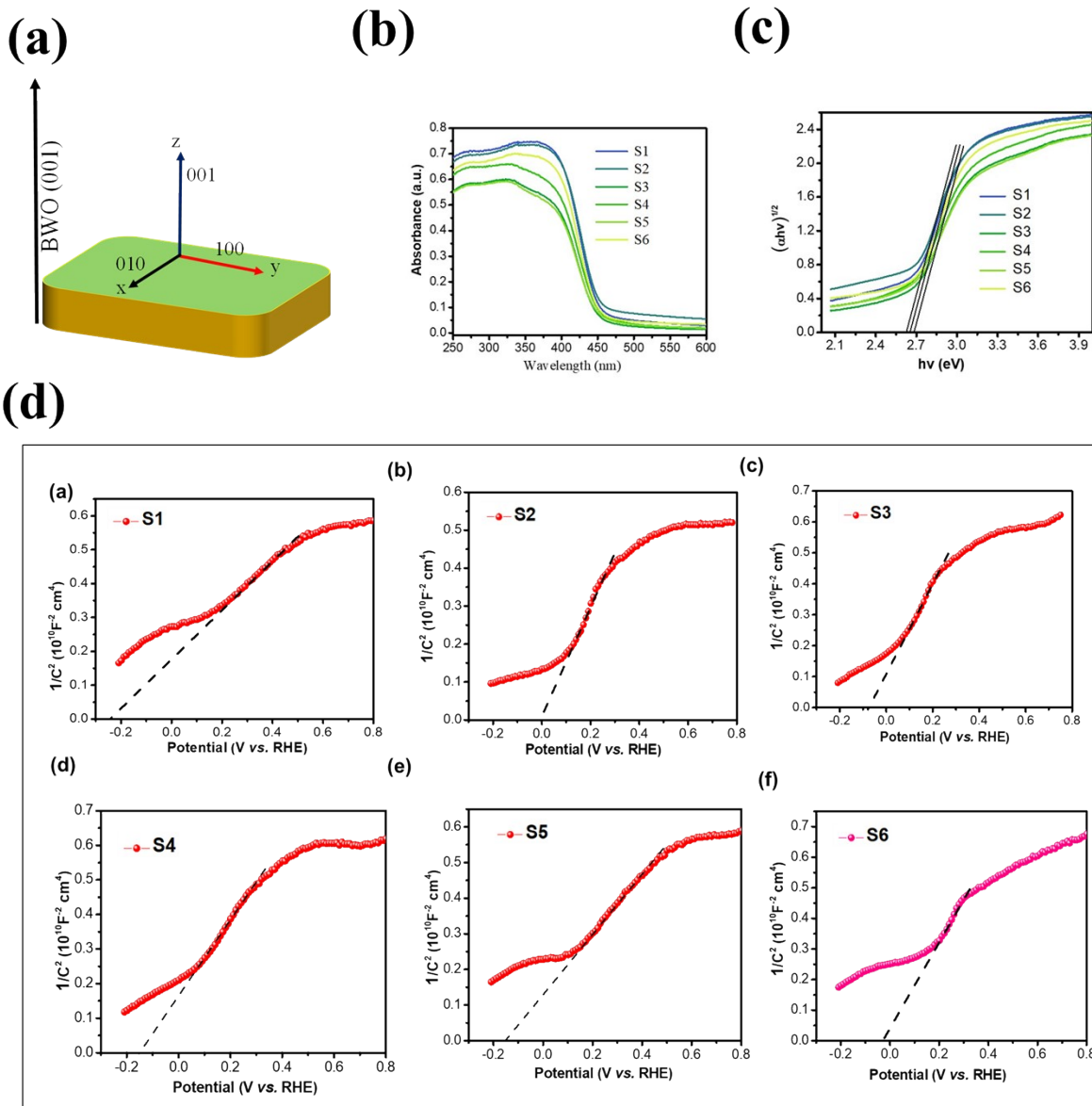


Fig. S12 (a) Schematic illustrations of Bi₂WO₆ crystal orientation; (b) DRS spectra of Bi₂WO₆ samples; (c, d) Tauc plot of $(\alpha h\nu)^{1/2}$ vs. $h\nu$ (eV) and Mott-Schottky plots of samples S1-S6.

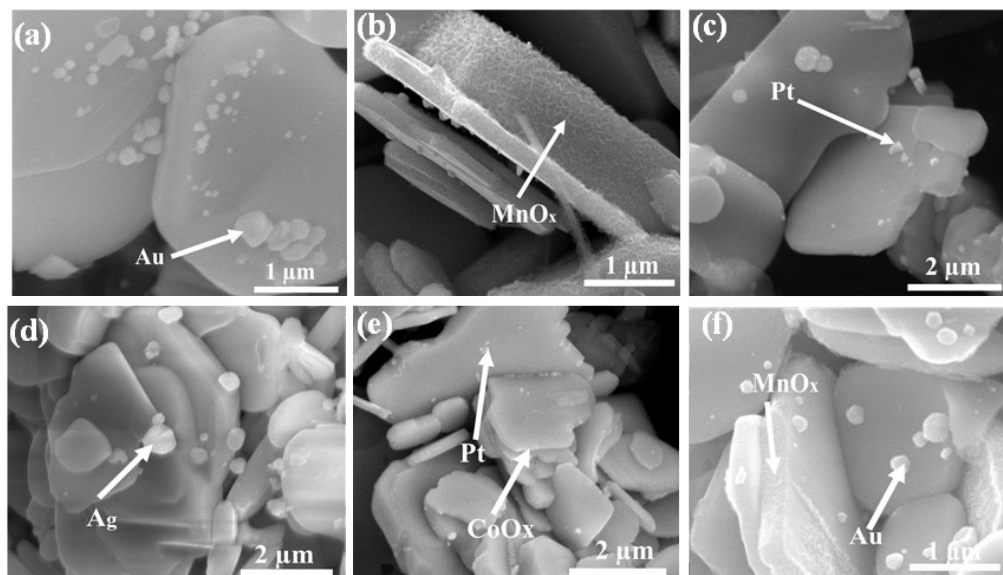


Fig. S13 SEM images of photo-deposition of noble metals and photo-deposition of metal oxides on Bi_2WO_6 nanoplates. (a) $\text{Au}/\text{Bi}_2\text{WO}_6$; (b) $\text{MnO}_x/\text{Bi}_2\text{WO}_6$; (c) $\text{Pt}/\text{Bi}_2\text{WO}_6$; (d) $\text{Ag}/\text{Bi}_2\text{WO}_6$; (e) $\text{Pt}/\text{CoO}_x/\text{Bi}_2\text{WO}_6$ and (f) $\text{Au}/\text{MnO}_x/\text{Bi}_2\text{WO}_6$.

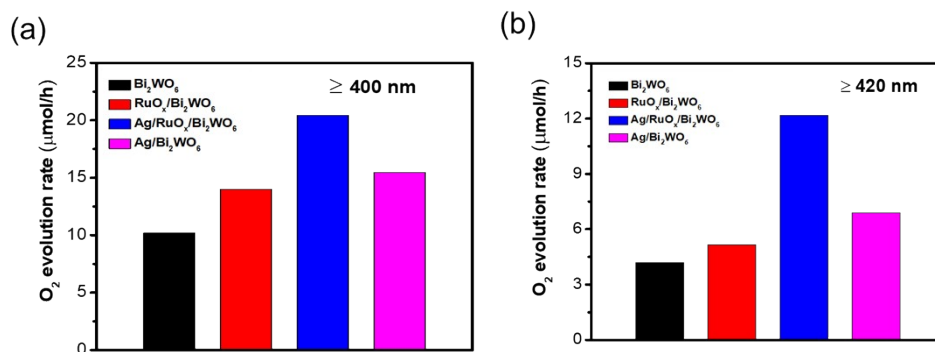


Fig. S14 Effect of cocatalyst on photocatalytic water oxidation of Bi_2WO_6 under different wavelength range. Reaction condition: catalyst, 100 mg; 1.0 mM $\text{Fe}(\text{NO}_3)_3$, 100 mL; light source, Xe lamp (300 W) fitted with a cut-off filter ($\lambda \geq 400$ nm and $\lambda \geq 420$).

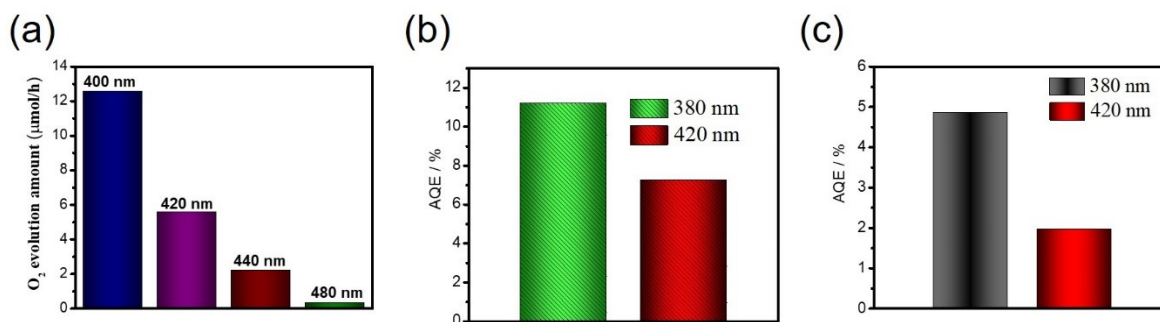


Fig. S15 (a) Show the effect of excitation wavelength on the Bi_2WO_6 charge separation process, (b) Apparent quantum efficiencies of photocatalytic Fe^{3+} conversion on the Bi_2WO_6 in methanol under different band-pass wavelength. Reaction conditions: catalyst 120 mg, 20 % methanol, 5.0 mM $\text{Fe}(\text{NO}_3)_3$, light source, Xe lamp (300 W) with $\lambda \geq 420$ nm and $\lambda \geq 380$ nm band-pass. (c) Apparent quantum efficiencies of Bi_2WO_6 for photocatalytic O_2 evolution from aqueous $\text{Fe}(\text{NO}_3)_3$ solution. Reaction conditions: catalyst 120 mg, 100 mL H_2O , 20 mL 5.0 mM $\text{Fe}(\text{NO}_3)_3$, light source, Xe lamp (300 W) with $\lambda = 420$ nm and $\lambda = 380$ nm band-pass

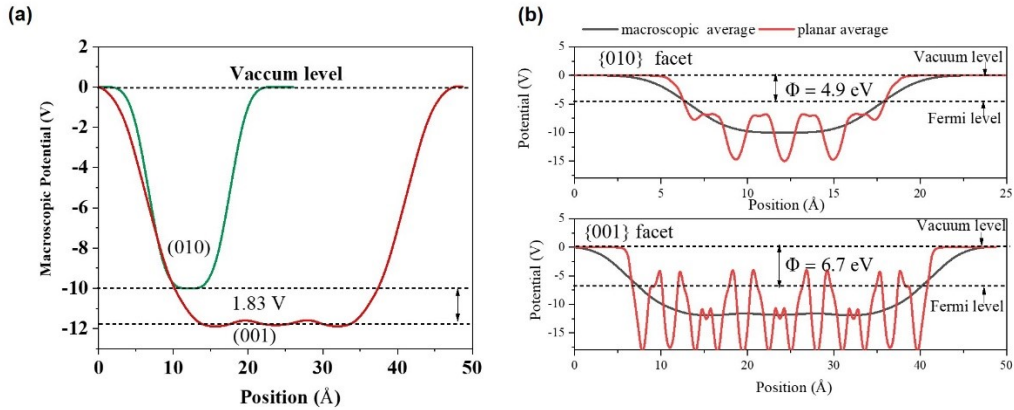


Fig.16 (a) Calculated macroscopic potential of Bi_2WO_6 {010} and {001} facet. (b) The electrostatic potentials for {010} and {001} facets of Bi_2WO_6 nanoplates. The red line and black line represent the planar and macroscopic average, respectively. The dashed line label the position of Fermi level and vacuum level, respectively.

To comprehend further the spatial charge separation between {001} and {010} facets of Bi_2WO_6 and understand the nature of band bending in Bi_2WO_6 crystal structure, DFT calculation analysis was adopted. The crystal structure analysis results show that, {010} facet is composed of W/Bi-O atomic arrangements while {001} facets composed of W-O atomic arrangement. Undoubtedly, the different in the surface atomic arrangement is capable of introducing a large surface dipole (work function difference). As shown in Fig. S16, our calculations results reveal that {001} facet have larger surface work function than that of {010} facet, which will create the oriented built-in electric field from {010} to {001} and drive efficient charge separation. The surface work-function difference between {001} and {010} facets also mean the different in surface band bending (Fig. 17). Based on the above analysis, the surface band bending of {010} facet is much larger than that of {001} facet, which is believed provide the driven force for spatial separating of photogenerated electrons and holes between {001} and {010} facets. Under the driving of oriented built-in electric field due to surface work function difference or band bending difference of two facets, holes preferably accumulate on {010} facet and vice versa, which is consistent with our photo-deposition probe experiments (Fig.3 and Fig. S13)^{12,13}. Moreover, the microcrystal thermodynamic trends to expose facet slabs with low surface energy, the large composition difference of the two facets are inevitably the causes of the surface energy difference. Our DFT calculations shows that {001} facets have lower surface energy than {010} facets (Table S4), therefore {001} facets should have larger exposed area.¹⁴ This is in good agreement with the SEM and TEM analysis.

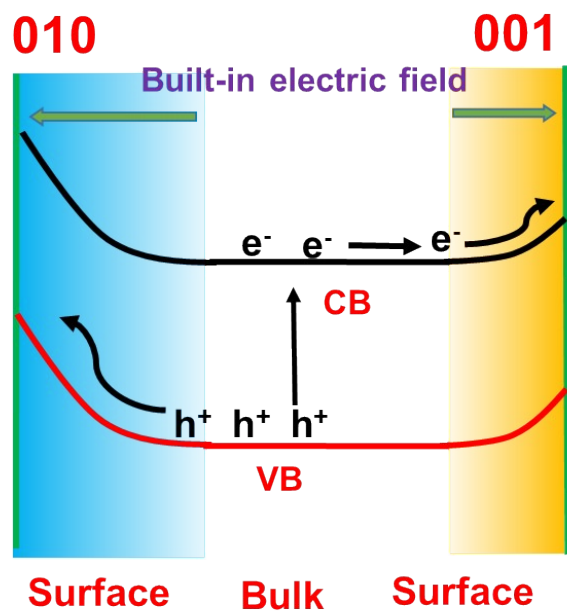


Fig. S17 Surface band bending of Bi_2WO_6 {010} and {001} facets.¹⁵

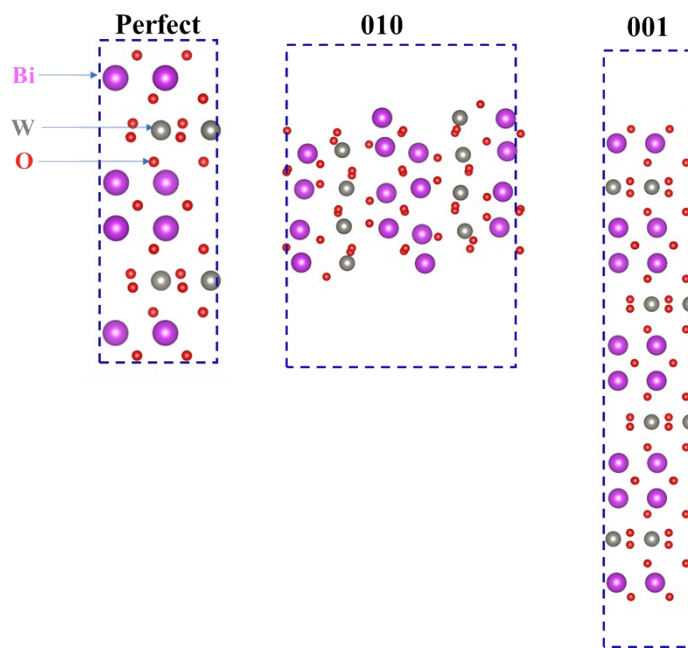


Fig. S18 Surface slab of different facets of unit Bi_2WO_6 crystal.

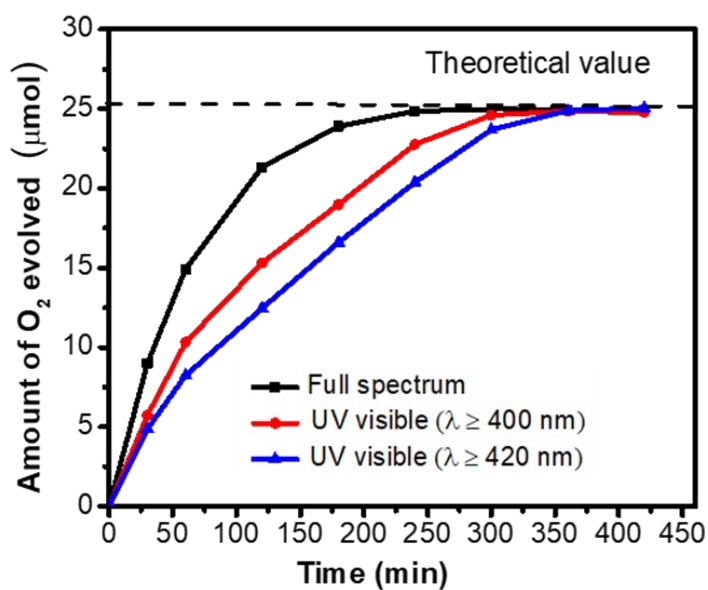


Fig. S19 Time course photocatalytic oxygen evolution on Bi₂WO₆ microplate under different wavelength ranges. Reaction conditions: catalyst, 100 mg, 100 mL H₂O, 1.0 mM Fe(NO₃)₃, light source, Xe lamp (300 W) fitted with cut-off filters (λ= 400 nm or λ= 420 nm). Reaction conditions: catalyst, 100 mg, 100 mL H₂O, 5.0 mM Fe(NO₃)₃, light source, Xe lamp, 300 W (λ= 420 nm).

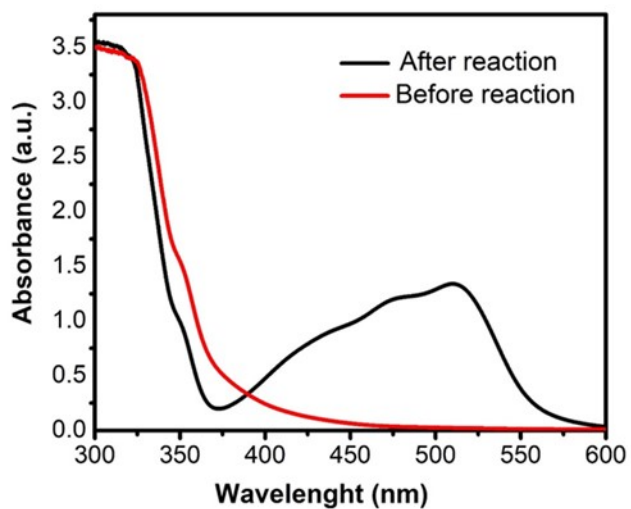


Fig. S20 UV-Vis's spectra of Fe²⁺ ion in solution before and after photocatalytic reaction determined using phenanthroline method.

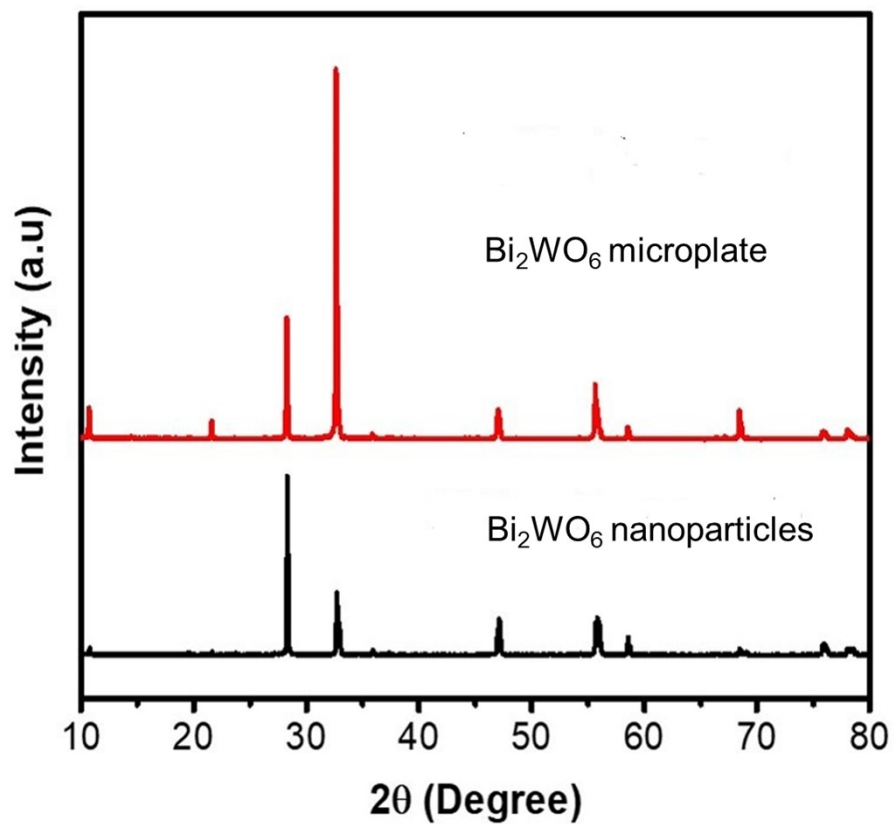


Fig. S21 XRD patterns of Bi_2WO_6 nanoparticle and microplate.

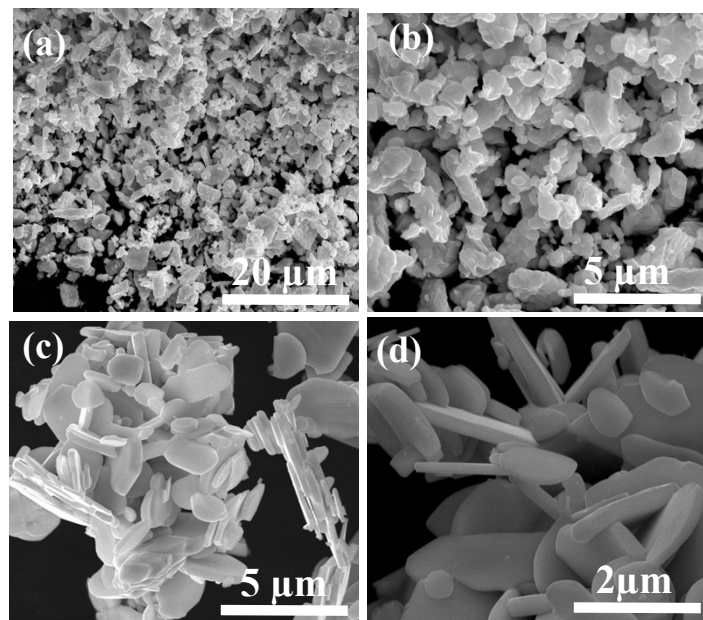


Fig. S22 SEM images of Bi_2WO_6 nanoparticle (a, b) and microplate (c, d)

Table S1. Crystal size and the surface area of flux prepared Bi₂WO₆ samples.

Sample name	Thickness (nm)	Surface area (m ² /g)
S1	511	3.7
S2	443	4.2
S3	356	4.8
S4	256	6.1
S5	226	6.7
S6	168	7.3

Table S2. Selected EDX results of Bi₂WO₆

Elements	Wt. %	Atomic (At) %
O	-	-
Bi	56.3150	17.3
W	27.9860	09.8

Table S3. EIS fitted results and the equivalent circuit used for fitting data entries in of the as-prepared Bi₂WO₆ samples from Fig. 2c.

sample	R1 / Ω	R2/ Ω
S1	52.95	183420
S2	50.37	124830
S3	35.56	97932
S4	30.98	65740
S5	28.68	57846
S6	33.50	73760

Table S4. Calculated lattice surface area, total energy, and surface energy.

System	Surface Area (nm ²)	Total Energy (eV)	Surface energy (eV)
Bulk		-267.8501	
001	0.3107	-531.9253	0.9720
010	0.9450	-502.4670	2.8134

References

- 1 R. Li, F. Zhang, D. Wang, J. Yang, M. Li, J. Zhu, X. Zhou, H. Han and C. Li, *Nat. Commun.*, 2013, **4**, 1432.
- 2 G. Kresse and J. Furthmuller, *Comput. Mater. Sci.*, 1996, **6**, 15-50.
- 3 P. E. Blochl, *Phys. Rev.*, B 1994, **50**, 17979.
- 4 J. P. Perdew, K. Burke and M. Ernzerhof, *Phys. Rev. Lett.*, 1996, **77**, 3868.
- 5 C. W. Kim, Y. S. Son, M. J. Kang, D. Y. Kim and Y. S. Kang, *Adv. Energy Mater.*, 2016, **6**, 1501754.
- 6 J. H. Zhang, F. Z. Ren, M. S. Deng and Y. X. Wang, *Phys. Chem. Chem.*, 2015, **17**, 10226.
- 7 C. Zhang and Y. Zhu, *Chem. Mater.*, 2005, **13**, 3537.
- 8 M. Maćzka, L. Macalik, and S. Kojima, *J. Phys. Condens. Matter.*, 2011, **23**, 405902.
- 9 X. Tao, Y. Gao, S. Wang, X. Wang, Y. Liu, Y. Zhao, F. Fan, M. Dupuis, R. Li and C. Li, *Adv. Energy Mater.*, 2019, **9**, 1803951.
- 10 A. Walsh, C. R. A. Catlow, *J. Mat. Chem.*, 2010, **20**, 10438.
- 11 L. Weston, H. Tailor, K. Krishnaswamy, L. Bjaalie, C. G. Van de Walle, *Comput. Mater. Sci.*, 2018, **151**, 174-180.
- 12 T. Takata, J. Jiang, Y. Sakata, M. Nakabayashi, N. Shibata, V. Nandal, K. Seki, T. Hisatomi, K. Domen, *Nature* 2020, 581, 411.
- 13 J. Zhu, S. Pang, T. Dittrich, Y. Gao, W. Nie, J. Cui, R. Chen, H. An, F. Fan, C. Li, *Nano letters* 2017, 17, 6735.
- 14 H. G. Yang, C. H. Sun, S. Z. Qiao, J. Zou, G. Liu, S. C. Smith, H. M. Cheng, G. Q. Lu, *Nature* **2008**, 453, 641.
- 15 D. Li, R. Chen, P. Wang, Z. Li, J. Zhu, F. Fan, J. Shi, C. Li, *ChemCatChem* 2019, 11, 3763-3769.